JELLINEK, F. (1961). *Nature* (*London*), **192**, 1065–1066.
JONGE, R. DE, POPMA, T. J. A., WIEGERS, G. A. & JELLINEK, F. (1970). *J. Solid State Chem.* **2**, 188–192.
KADIJK, F., HUISMAN, R. & JELLINEK, F. (1968). *Acta Cryst.* B**24**, 1102–1109.
KADIJK, F. & JELLINEK, F. (1969). *J. Less-Common Met.* **19**, 421–430.
MCCABE, C. L. (1955). *J. Met.* **7**, 61.
PAULING, L. (1960). *The Nature of the Chemical Bond.* Ithaca: Cornell Univ. Press.
RASTOGI, A. K. (1985). *Philos. Mag. B*, **192**, 909–919.
SLATER, J. C. (1964). *J. Chem. Phys.* **41**, 3199–3204.
YAMAMOTO, A. (1985). *REMOS85.0. Computer Program for the Refinement of Modulated Structures.* National Institute for Research in Inorganic Materials, Sakura-Mura, Niihari-Gun, Ibaraki 305, Japan.

Acta Cryst. (1993). B**49**, 794–806

X–N Study of the Electron Density in $(ND_4)_2Cu(SO_4)_2.6D_2O$ at 9 K: Flexible Radial Functions are Vital

BY BRIAN N. FIGGIS

Department of Chemistry, University of Western Australia, Nedlands, WA 6009, Australia

BO B. IVERSEN AND FINN K. LARSEN

Department of Chemistry, Aarhus University, DK 8000, Aarhus C, Denmark

AND PHILIP A. REYNOLDS

Department of Chemistry, University of Western Australia, Nedlands, WA 6009, Australia

(*Received* 4 *December* 1992; *accepted* 17 *March* 1993)

Abstract

Diammonium hexaaquacopper(II) disulfate-d_{20}, $[ND_4]_2[Cu(D_2O)_6](SO_4)_2$, $M_r = 419.7$, monoclinic $P2_1/a$, $a = 9.393$ (2), $b = 12.666$ (2), $c = 6.061$ (1) Å, $\beta = 107.16$ (1)°, $V = 689.0$ (4) Å^3, $Z = 2$, Mo $K\alpha$ radiation, $\lambda = 0.71069$ Å, $\mu = 2.01$ mm^{-1}, $F(000) = 415.3$ (414.0 without anomalous dispersion), $T = 9$ (1) K, $R(I) = 0.013$, $R(F) = 0.0095$, $\chi^2 = 0.89$, 5134 reflections. Refinement of the X-ray data, using a radially augmented multipolar charge model, gave thermal and positional parameters agreeing with those derived from neutron diffraction data and the correct cell content of electrons. The mean diagonal thermal-parameter difference between X-ray and neutron results is only 0.0003 Å^2. Two factors are vital in obtaining satisfactory and consistent fits to both experiments. (1) The use of a very low (< 10 K) temperature to eliminate thermal diffuse scattering and anharmonic effects, which are important even at 85 K. (2) The use of an electron-density model which includes more than one component in the atom-centred radial distributions; a single parameter 'κ' refinement is *not* adequate. The charge-density model is consistent with that obtained previously at 85 K, but is more precise, and uncertainties from possible systematic errors are much reduced. A simple valence model of the charge density, while still a good approximation, is no longer adequate. The reduced thermal motion at 9 K and use of neutron data reveal radial and angular density features which were not seen at 85 K, and which are inconsistent with simple valence models. However, they agree well with high-quality *ab initio* theoretical calculations. In particular, deep holes near the O and S nuclei are present in the theoretical maps, and are also significant in the experimental maps.

Introduction

The diammonium hexaaquametal(II) disulfates, examples of the Tutton salts, are excellent subjects for the study of metal–water bonding, and also of hydrogen bonding. The current state of our X-ray and polarized neutron diffraction (PND) studies of these systems, and other relevant experiments, have been summarized by Figgis, Khor, Kucharski & Reynolds (1992). That paper presented an X-ray diffraction study of the copper member of this series at 85 K. It showed the Jahn–Teller distortion of the copper 3*d* shell and both σ and π charge flow from the sulfate ion through water molecules to the Cu atom. The metal–water bonding found agreed quite well with theoretical calculations (Chandler, Christos, Figgis & Reynolds, 1992), but expected features such as lone pairs were not well resolved. In addition, substantial anharmonicity, connected with

Acta Crystallographica Section B
ISSN 0108-7681 ©1993

the Jahn–Teller distortion, was present, particularly concerning the Cu atom.

Here, we have repeated this experiment at the much lower temperature of 9 K, for two reasons. Firstly, reduction in thermal motion should reduce thermal smearing of the static charge density enough to reveal new features, and it may also suppress anharmonic and thermal diffuse-scattering (TDS) effects on the deformation density. Secondly, the reduction in anharmonicity and TDS should allow a useful comparison with the very low temperature (15 K) neutron diffraction data which we have available (Iversen, Larsen, Figgis & Reynolds, 1993). We have shown by a high-resolution neutron diffraction experiment on cobalt phthalocyanine that, except for the most rigid substances, *X–N* comparisons at liquid-nitrogen temperatures still contain serious errors as a result of TDS and anharmonicity (Reynolds, Figgis, Kucharski & Mason, 1991). We show that both expectations are realized, and that, although consistent with the 85 K data, the 9 K data are a substantial improvement.

Experimental

A pale-blue deuterated (86%, determined by the neutron diffraction experiment and NMR) crystal, prepared by repeated recrystallization of the hydrogenous salt from D_2O, of dimensions from an arbitrary centre $\pm(110)$ 0.20, $\pm(10\bar{1})$ 0.21, $\pm(1\bar{1}0)$ 0.16, $\pm(101)$ 0.21, $\pm(011)$ 0.24, $\pm(01\bar{1})$ 0.22, (010) 0.27 mm, was mounted on a type 512 Huber four-circle diffractometer fitted with a type 202 Displex refrigerator operating at 8.7 (4) K (Henriksen, Larsen & Rasmussen, 1986) with *b* almost parallel to the Displex axis. Graphite-monochromatized Mo $K\alpha$ radiation was employed. The unit cell was determined by least-squares fitting of the setting angles of 30 well spaced reflections with $31 < |2\theta| < 55°$, centred at both positive and negative values of 2θ. A sphere of data was collected in the region $2\theta < 60°$ and almost two quadrants with $60 < 2\theta < 100°$, plus thin shells around $2\theta = 70, 80, 85, 100°$. The intense data were recollected at a reduced generator voltage. Finally, two spheres of data with $2\theta < 30°$, but ψ differing by 1° were collected. An ω–2θ scan was used with width, $\Delta\theta$, at values of θ as follows: 1.20, 0; 1.30, 15; 1.50, 30; 2.00, 45; 2.60, 60°. Collimation was tight, so that the background rate was only ~ 1 count s^{-1}, compared to peak-height maxima in excess of 10 000 counts s^{-1}. The range of the data was: $[(\sin\theta)/\lambda]_{\max} = 1.09$ Å^{-1}, $|h| < 21$, $|k| < 19$, $|l| < 12$.

21 462 reflections were measured, using three standards every 50 reflections, and periodic recentring. The standards showed a decay of about 5% in intensity over the 10 week data-collection period. At higher 2θ and high χ the crystal moved partly out of the beam, presumably because of the torque produced by the then almost horizontal Displex. This effect commenced quite suddenly at $k \simeq 22$–24. Conservatively, we have removed all data with $k > 18$. Thus our unique data is complete only to 0.7 Å^{-1}, and relatively complete to ~ 0.8 Å^{-1}. Integrated intensities were extracted from the raw data by use of the profile-analysis program *COLL5N* (Lehmann & Larsen, 1974) [based on the minimization of $\sigma(I)/I$], normalized to the standards, and a Gaussian absorption correction (512 points) was applied with the *DATAP* program (Coppens, Leiserowitz & Rabinovich, 1965) (maximum and minimum transmission of 0.59 and 0.48). 19 874 data were sorted and averaged. Outliers in the averaging of the equivalent reflections were rejected, to give 5160 unique reflections. The agreement of equivalents was $R_{\rm int}(I) = 0.020$. The rejected outliers were mainly weak reflections which had higher intensity than several other agreeing equivalents. We also note that the formally absent reflections often had intensities of about the magnitude of the intensity differences between rejected reflections and the average, consistent with multiple scattering. Harmonic contamination of the radiation seemed unimportant, as the 'forbidden' intensity showed no correlation with the structure factor at twice the wavevector. Lastly, in the two inner spheres, differing in ψ, the weaker reflections sometimes had extra intensity in one or other set, apparently at random. This is all evidence that the major remaining error of the data is multiple scattering. We should, in hindsight, have used a crystal of less than about half the mass of that studied. Multiple scattering, contrary to TDS or anharmonicity, increases its relative effect as temperature is lowered.

Refinements

Previous model

Initially, we refined the data using the same model as for the 85 K data. This contains anisotropic harmonic temperature factors, except for deuterium, isotropic, and quartic isotropic anharmonic thermal parameters for all atoms except D and Cu. No anharmonic parameters were employed for D atoms, but on Cu atoms the full set of 15 quartic anharmonic parameters were introduced. Corrections were made for type II extinction (Becker & Coppens, 1974) and for multiple scattering (Le Page & Gabe, 1979; Figgis, Kucharski & Reynolds 1989), using a refinable two-parameter function (m_1, m_2) in the latter case

$$I(\text{obs}) = I(\text{calc}) + m_1 + m_2(1 - |\mathbf{k}|),$$

where **k** is the wavevector in Å^{-1}. The charge-density model for the 85 K data had $3d$ and $4p$ functions on Cu, (sp) hybrid orbitals on S, N and O, $1s$ on deuterium, and Gaussian functions in the S—O and Cu—O mid-bond points to allow for overlap density.

The relationship of this model to a conventional multipole model has been described in detail previously (Figgis, Reynolds & Wright, 1983). We summarize the difference between the valence and the multipole models as different treatments of spherical harmonic components in the atomic form factors, but the latter are summed in the same way to provide calculated reflection intensities.

For the multipole model

$$f(\kappa) = f_{\rm core} + \sum_{nln'l'} \sum_{l''m''} c^{nln'l'}_{l''m''} Y^{l''}_{m''}(\theta,\varphi)\langle j^{nln'l'}_{m''}(|\kappa|)\rangle,$$

where $f(|\kappa|)$ is the atomic fragment form factor, $f_{\rm core}(|\kappa|)$ is the core form factor and $nln'l'$ are two sets of atomic quantum numbers, and there are sets of multipoles specified by l'' up to order m''. The $c^{nln'l'}_{l''m''}$ are refinable coefficients and the $Y^{l''}_{m''}(\theta, \varphi)$ are spherical harmonics defined with the phase convention of Condon & Shortley (1957). The $\langle j^{nln'l'}_{m''}(|\kappa|)\rangle$ are shell form factors, which have been variously defined. We chose the definition in terms of the overlap of the radial parts of two Hartree–Fock atomic wavefunctions, $R_{nl}(r)$, with principal and angular quantum numbers nlm and $n'l'm$.

$$\langle j^{nln'l'}_{m''}(|\kappa|)\rangle = \int r^2 R_{nl}(r) R_{n'l'}(r) j_{m''}(|\kappa|r){\rm d}r,$$

where $j_{m''}(|\kappa|r)$ is the spherical Bessel function of order m''.

By linear transformations, the resulting multipole coefficients, $c^{nln'l'}_{l''m''}$, can be related to populations of functions relating to the overlaps of atomic functions [for the d–d orbital case see Varghese & Mason (1980)]. This is the 'valence-orbital population' model. For example, the overlap $\langle d_{xy}|d_{z^2}\rangle$ contains terms in j_0^{3d3d}, j_2^{3d3d} and j_4^{3d3d} in a definite ratio. The ratio may be expressed in terms of the standard $3-j$ symbols $c^{l''m''}(lm,l'm')$ (Weiss & Freeman, 1959; Condon & Shortley, 1957), so that we can refine populations of such overlap functions. We do that here with the variables $C_{nlm,n'l'm'}$,

$$f(\kappa) = f_{\rm core} + C_{nlm,n'l'm'} \sum_{m''l''} [8m'' + 4]$$
$$\times\, \pi i^{m''} c^{l''m''}(lm,l'm')\, Y^{l''}_{m''}(\theta,\varphi)\langle j^{nln'l'}_{m''}(|\kappa|r)\rangle.$$

We then are able, for example, to refine 'd-orbital' populations directly. The two models, valence and multipole, are, in the limit of $m''l''$ summed to infinity, identical. The valence model, for finite series, has the advantage that the terms expected to be large on the grounds of theoretical chemical calculations, can be selected for consideration at the expense of those expected to be small, thus reducing the size of the problem.

The radii of non-D atoms were allowed to vary in the usual κ refinement manner (Coppens, Guru-Row, Leung, Stevens, Becker & Yang, 1979). Scattering factors were calculated for core and valence functions from the atomic wavefunctions of Clementi & Roetti (1974) using the program *JCALC* (Figgis, Reynolds & White, 1987), except for D, where the function of Stewart, Davidson & Simpson (1965) was used. The anomalous-dispersion corrections of Kissel & Pratt (1990), modifying those of Cromer & Liberman (1970), were applied. All data were used in minimizing the function $\sum\{\sigma(I)^{-2}[I({\rm obs}) - I({\rm calc})]^2\}$ until the maximum shift/e.s.d. was less than 0.1. The refinement program was *ASRED* (Figgis, Reynolds & Williams, 1980).

This 229 variable model gave $R(I) = 0.0152$, $R(F)$ $[I > 3\sigma(I)] = 0.0110$ and $\chi^2 = 1.040$. The maximum extinction effect calculated was a 5% reduction in intensity. The model provides an excellent fit, with χ^2 lower than for the 85 K data. Of the 33 reflections which fit worst $\{d = |[I({\rm obs}) - I({\rm calc})]|/\sigma(I) > 3\}$, 30 had $I({\rm obs}) > I({\rm calc})$, and only three $I({\rm obs}) < I({\rm calc})$. All were weak in intensity. This again is a sympton of multiple scattering. Most of these reflections were derived from only one or two equivalents, and so had not been rejected in the averaging. We reject the 27 with $d > 3.5$ in further refinement.

The charge-density model parameters follow those at 85 K well, and confirm the conclusions of Figgis *et al.* (1992). The anharmonic parameters on Cu and S atoms are, however, not significant at this lower temperature, while those on O and N atoms are much reduced. No particular subset of the reflections is especially sensitive to anharmonic effects in this crystal. It is pleasing to confirm that the charge-density information obtained at 85 K is fairly reliable, even in the presence of anharmonicity so large that it swamps many other effects in the deformation-density maps. The deformation density is defined as the difference between the total charge density and a model density consisting of the sum of atomic contributions smeared by the observed thermal motion. It thus reflects the changes in the charge density on assembling a set of atoms to form the crystal.

Radial and angular deficiency of previous model

However, at the lower temperature, and with the use of the available 15 K neutron thermal parameters, we find that the above model has a number of defects. They include the fact that high- and low-angle refinements gave thermal parameters differing by 10–15% for O and N, but not Cu and S. Also, the total electron count deduced for the unit cell was 4% too high. Such results are often observed, also, when analysing data from higher temperatures. They are recognized to arise at least partly from the different way in which TDS affects the X-ray and the neutron-scattering experiments and in the neglect of anharmonicity in the thermal motion. However, at the low temperature of this experiment both effects must be small and we are justified in comparing the thermal parameters from the X-ray and the neutron diffraction experiments, and thus deciding whether there is a defect in the charge-density model or in the thermal-motion model. The high-angle structural and thermal parameters from the X-ray experiment agree with those from the neutron data within the errors, but those from the low-angle data do not. This indicates that the charge-density model is deficient. It needs to be made more flexible in relation to the O-atom and N-atom sites.

An examination of residual maps, which are derived from the difference between the observed and the model intensities, indicates that around the N and O atoms there is density corresponding to multipoles of order 3 and 4. The simple chemically inspired *sp* hybrid-orbital scheme of the previous model is restricted to second-order multipoles. The new data evidently require the consideration of effects not provided for in such simple chemical modelling. The molecular density is not described by simple κ modification of atomic radial functions.

New model

To provide more radial flexibility on each N-atom and O-atom site we added two functions which transfer density from more diffuse regions to those closer to the nucleus, or *vice versa*, on molecule formation. We define a wavefunction $|S1\rangle$ as a Slater-type oribital (STO) function with the smallest exponent appearing in the Clementi & Roetti (1974) atomic wavefunction, corresponding to the most diffuse function. $|S2\rangle$ has the second smallest such exponent. We then refined populations of the functions $\langle S1|S1\rangle - \langle S1|S2\rangle$ and $\langle S1|S2\rangle - \langle S2|S2\rangle$. This provides a means of changing the radial dependence in the diffuse regions of the atoms independently of κ. One better chosen extra radial function might be sufficient, but we decided to provide as much flexibility as reasonably possible since we were unsure of the nature of the changes which might be required. The total density will be relatively unaffected, even if the two additional parameters are quite correlated. In addition, for consistency, we use the deuterium nuclear positions determined by the neutron diffraction experiment. This also requires more flexibility in the model, so we employed two STO 1*s* distributions on each D atom, with exponents, ζ, of 1.0 and 0.5. The Cu valence distribution did not need to be modified, since the diffuse 4*p* orbital was already present. On S we added only a $\langle S1|S1\rangle$ density, since the $n = 3$ shell is already quite diffuse.

To increase the angular flexibility we used multipolar functions instead of the previous chemically based model. Initially, we restricted the multipoles refined to those of order 4 or less, and κ modified only the main radial functions (Cu 3*d*, O and N 2*s*/*p*, S 3*s*/*p*). We restricted the additional angular functions to those allowed in the approximate local site symmetry: Cu *mmm*, S and N $\bar{4}3$, O3—O6 and D cylindrical, and O7—O9 *m*. In addition, on Cu we allowed $4p_x$, $4p_y$ and $4p_z$ functions and only multipoles 00, 10 and 20 on D.

We used the positional and thermal parameters for the D atoms determined by the neutron diffraction experiment. However, we decided to refine those parameters for the non-D atoms, since they are well determined by the X-ray data and are not much correlated with the electron-density model. This produre, a partial *X*–*X* refinement, allows a comparison of these parameters between the two diffraction experiments, and gives a further check on the adequacy and soundness of the modelling.

This new extended model proved to be sufficient. The refinements of the high- and low-angle data give similar thermal parameters and scale factors. Our use, in this refinement, of the correct cell content of electrons does not degrade the fit, and the agreement factors improve appreciably over the previous treatment. This 283-variable model gives $R(I) = 0.0130$, $R(F)$ $[I > 3\sigma(I)] = 0.0095$ and $\chi^2 = 0.890$ for 5134 data. The residual density is almost featureless, with extrema of -0.21 and 0.16 e Å^{-3} when summed to a resolution of 0.8 Å^{-1}. The *poorest* fragment plane is Cu—O(7)—O(8), which is shown in Fig. 1. The -0.21 e Å^{-3} extremum lies close to this plane, but not in it.

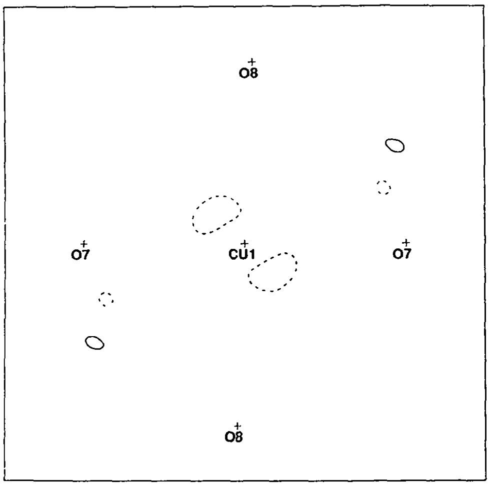

Fig. 1. Experimental residual density in the Cu—O(7)—O(8) plane. Contour interval is 0.1 e Å^{-3}. Positive, solid lines; negative, dashed lines; zero and values > 1.9 and < -1.1 e Å^{-3} suppressed. Box size 5.98 Å, square. Resolution 0.8 Å^{-1}.

The final non-D positional and thermal parameters are given in Tables 1 and 2.*

The final model differs from the initial valence model in four respects. They are:

(*a*) The cell contents are constrained to be the correct number of electrons according to the chemical formula.

(*b*) The H atoms are described by functions centred on the true nuclear positions, rather than the X-ray refined positions.

(*c*) Extra angular functions are introduced on most atoms.

(*d*) Extra radial functions are introduced on some atoms.

The source of the improvement in the agreement factors can be illustrated by the use of intermediate refinements. Fixing the H-atom positions at the neutron-structure values would seriously degrade the fit if it were not for the augmentation of the H-centred functions by dipolar and quadrupolar terms. When those are present, the fit is virtually unaltered from that for the X-ray-refined H-atom positions. Similarly, the addition of extra angular functions, while required to improve the deformation-density maps, does not markedly improve the fits. This is illustrated by a refinement which differs from the final one in only two respects. These are that the diffuse populations centered on N, O and S atoms are set to zero, and that the cell content of electrons is not constrained to the formula value. This results in a fit very similar to that of the valence model. The fit parameters are $R(I) = 0.0166$, $R(F)$ $[I > 3\sigma(I)] = 0.0113$, $\chi^2 = 1.074$ and the cell is projected to contain 5.7% too many electrons. If the cell content is constrained to be correct, then under these conditions, the fit degrades, to $R(I) = 0.0185$, $R(F)$ $[I > 3\sigma(I)] = 0.0118$, $\chi^2 = 1.129$, with the 5134 data.

Allowing the N, O and S diffuse function to vary, the final model, improves the fit considerably and gives the correct cell contents. It is clear that the major improvement in modelling that we have made is to allow extra flexibility in the diffuse functions centred on the N, O and S atoms. The other changes in the valence model, while invoked for good reasons such as consistency with the neutron structural results, do not significantly improve the fit to our X-ray data.

Table 1. *Comparison of* X-*ray and neutron positional parameters* ($\times 10^5$) *for deuterated copper Tutton salt at very low temperatures*

Neutron data (15 K) first entry, X-ray data (9 K) second entry.

				Difference/e.s.d.		
	x	*y*	*z*	*x*	*y*	*z*
S(2)	38679 (10)	14367 (7)	74919 (14)			
S(2)	38691 (1)	14365 (1)	74930 (1)	−1.2	0.3	−0.8
O(3)	38031 (5)	23865 (4)	60589 (8)			
O(3)	38041 (3)	23869 (3)	60585 (4)	−1.6	−0.8	0.4
O(4)	52759 (5)	08709 (4)	77544 (8)			
O(4)	52762 (3)	08708 (2)	77538 (4)	−0.6	0.2	0.7
O(5)	26101 (5)	07336 (4)	63022 (7)			
O(5)	26086 (3)	07334 (2)	63020 (4)	2.8	0.4	0.2
O(6)	37316 (5)	17338 (4)	97856 (7)			
O(6)	37304 (2)	17341 (2)	97866 (4)	2.3	−0.7	−1.2
O(7)	15153 (5)	10746 (4)	16484 (8)			
O(7)	15148 (3)	10756 (3)	16478 (4)	0.9	−2.0	0.7
O(8)	−18069 (5)	11197 (4)	05041 (8)			
O(8)	−18066 (3)	11193 (2)	05055 (5)	0.5	0.9	−1.4
O(9)	00999 (5)	−06612 (4)	29670 (8)			
O(9)	01005 (3)	−06613 (2)	29679 (4)	−1.2	−0.2	−1.0
N(10)	12603 (3)	36448 (2)	37800 (5)			
N(10)	12605 (3)	36450 (3)	37802 (4)	−0.4	−0.7	−0.3

Table 2. *Comparison of* X-*ray and neutron thermal parameters* ($Å^2 \times 10^5$)

Neutron data (15 K) first entry, X-ray data (9 K) second entry, difference/e.s.d. data third entry.

	U_{11}	U_{22}	U_{33}	U_{12}	U_{13}	U_{23}
Cu(1)	294 (19)	322 (19)	305 (16)	−20 (7)	73 (7)	1 (7)
	284 (2)	326 (3)	272 (2)	−26 (3)	75 (1)	19 (2)
	0.4	−0.2	2.0	−0.7	−0.3	−2.5
S(2)	304 (36)	324 (37)	362 (33)	−12 (15)	107 (14)	−6 (14)
	263 (3)	303 (5)	283 (3)	−13 (2)	70 (2)	0 (2)
	1.6	0.6	2.4	−0.1	2.6	−0.5
O(3)	740 (20)	445 (18)	609 (17)	−27 (8)	109 (7)	69 (7)
	705 (8)	475 (13)	563 (6)	−48 (7)	131 (5)	125 (8)
	1.6	−1.4	2.6	1.9	−2.2	−5.3
O(4)	386 (18)	702 (19)	747 (18)	60 (8)	109 (7)	11 (7)
	399 (8)	728 (12)	690 (7)	131 (8)	147 (5)	20 (6)
	−0.7	−1.2	3.0	−6.3	−4.4	−1.0
O(5)	452 (18)	530 (19)	588 (17)	−85 (7)	93 (7)	−52 (7)
	450 (7)	558 (12)	546 (6)	−127 (8)	106 (5)	−74 (6)
	0.1	−1.2	2.3	4.0	−1.5	2.4
O(6)	661 (19)	654 (19)	462 (16)	−21 (8)	140 (7)	−50 (7)
	648 (8)	679 (13)	389 (7)	−26 (6)	197 (5)	−89 (6)
	0.7	−1.1	4.2	0.5	−6.6	4.2
O(7)	542 (20)	733 (20)	588 (19)	−97 (8)	95 (8)	−5 (7)
	588 (7)	725 (13)	513 (6)	−196 (8)	114 (6)	−20 (6)
	−2.2	0.3	3.8	8.8	−1.9	1.6
O(8)	551 (22)	615 (23)	834 (18)	30 (8)	130 (8)	12 (7)
	589 (8)	655 (13)	804 (7)	34 (7)	185 (6)	50 (6)
	−1.6	−1.5	1.6	−0.5	−5.5	−4.1
O(9)	574 (20)	543 (21)	539 (16)	25 (8)	139 (7)	41 (7)
	576 (8)	544 (12)	506 (6)	28 (6)	211 (5)	87 (6)
	−0.1	0.0	2.0	−0.3	−8.4	−5.0
N(10)	651 (13)	681 (13)	667 (12)	3 (5)	136 (5)	13 (5)
	590 (8)	665 (14)	628 (7)	−3 (8)	192 (6)	30 (6)
	4.2	0.8	2.8	0.6	−7.2	−2.2

The deformation-density maps, obtained from the experimental data, are shown in Figs. 2–11 for the Cu—O(7)—O(8), Cu—(7)—O(9), Cu—O(8)—O(9), S—O(3)—O(4), S—O(5)—O(6), N—H(11)—H(12), N—H(13)—H(14), O(7)—H(15)—H(16), O(8)—H(17)—H(18) and O(9)—H(19)—H(20) planes, again to a resolution of 0.8 $Å^{-1}$, since the data are noticeably incomplete beyond that value. We demonstrate the quality of these maps by examining the O—H bond peaks which here are 0.5–0.65 e $Å^{-3}$ at the maxima. Previous experiments reach only 0.3 e $Å^{-3}$ (Hermannson, 1984). This improvement is the effect of the lower thermal motion caused by a combination of 9 K in temperature, together with deuteration. As we discuss later, this result allows much more reliable extrapolation to static density maps.

---

* Lists of intensities have been deposited with the British Library Document Supply Centre as Supplementary Publication No. SUP 71039 (12 pp.). Copies may be obtained through The Technical Editor, International Union of Crystallography, 5 Abbey Square, Chester CH1 2HU, England. [CIF reference: HL0025]

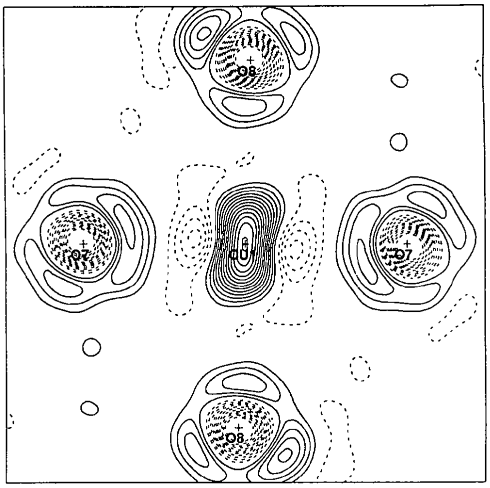

Fig. 2. Experimental deformation density in the Cu—O(7)—O(8) plane. Contours, size and resolution as for Fig. 1.

Fig. 5. Experimental deformation density in the S—O(3)—O(4) plane. Contours, size and resolution as for Fig. 1.

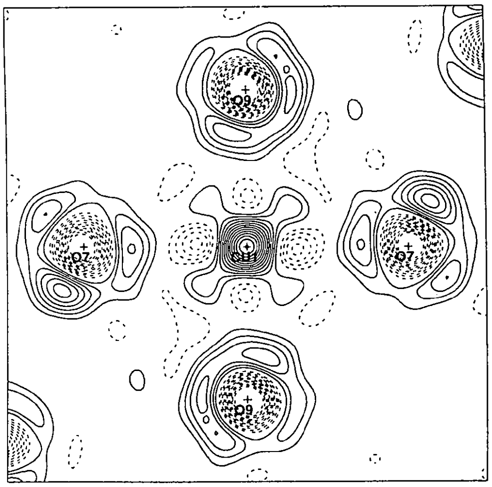

Fig. 3. Experimental deformation density in the Cu—O(7)—O(9) plane. Contours, size and resolution as for Fig. 1.

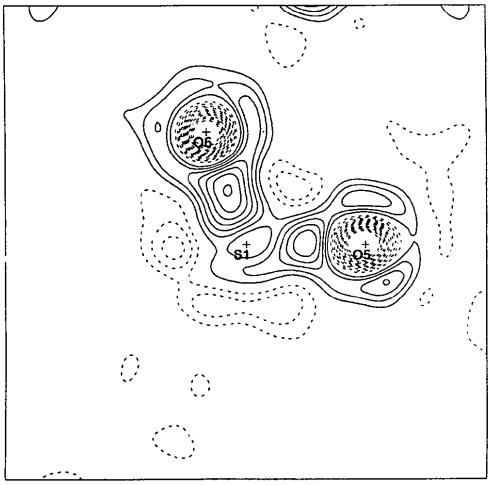

Fig. 6. Experimental deformation density in the S—O(5)—O(6) plane. Contours, size and resolution as for Fig. 1.

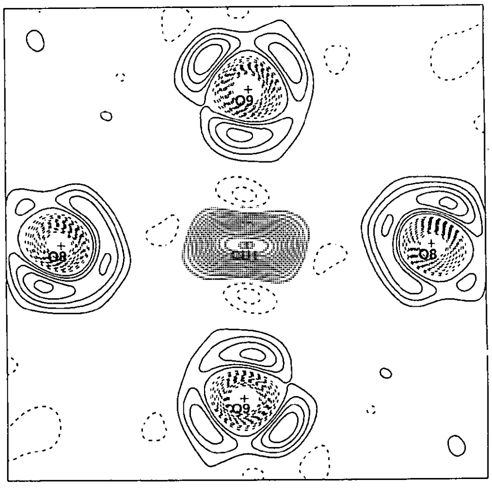

Fig. 4. Experimental deformation density in the Cu—O(8)—O(9) plane. Contours, size and resolution as for Fig. 1.

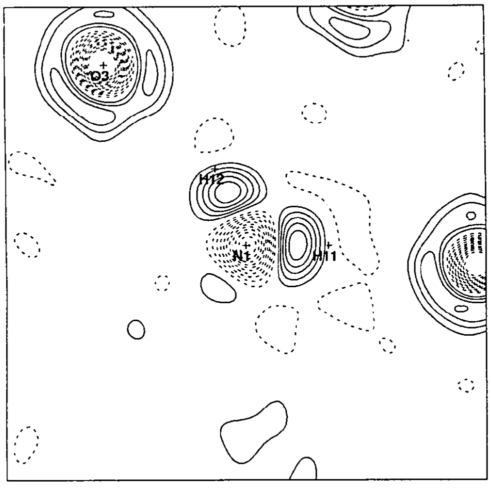

Fig. 7. Experimental deformation density in the N—H(11)—H(12) plane. Contours, size and resolution as for Fig. 1.

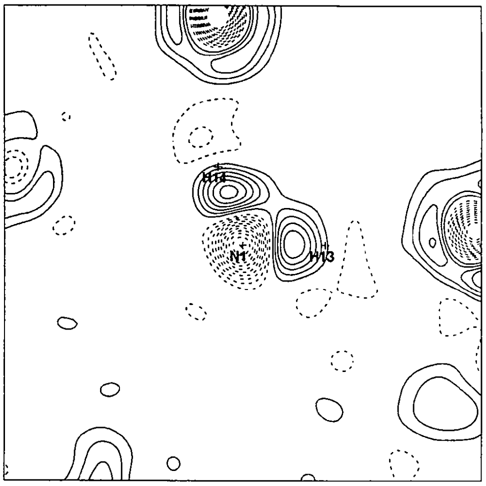

Fig. 8. Experimental deformation density in the N—H(13)—H(14) plane. Contours, size and resolution as for Fig. 1.

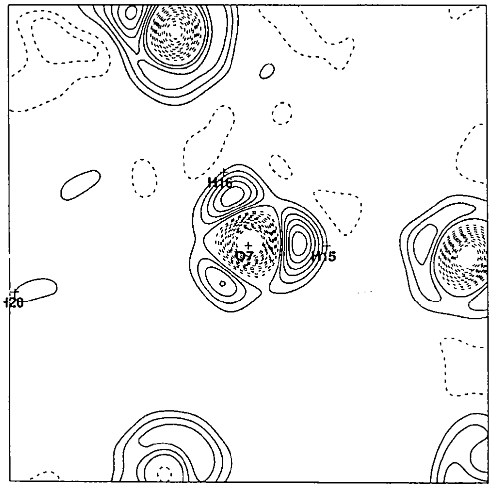

Fig. 9. Experimental deformation density in the O(7)—H(15)—H(16) plane. Contours, size and resolution as for Fig. 1.

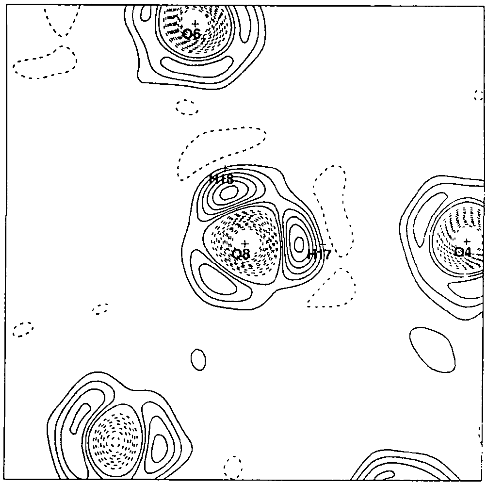

Fig. 10. Experimental deformation density in the O(8)—H(17)—H(18) plane. Contours, size and resolution as for Fig. 1.

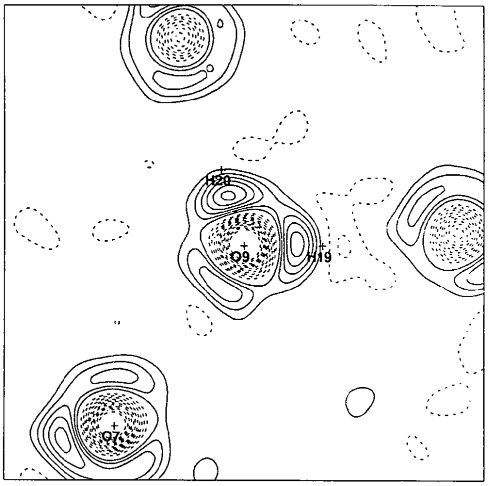

Fig. 11. Experimental deformation density in the O(9)—H(19)—H(20) plane. Contours, size and resolution as for Fig. 1.

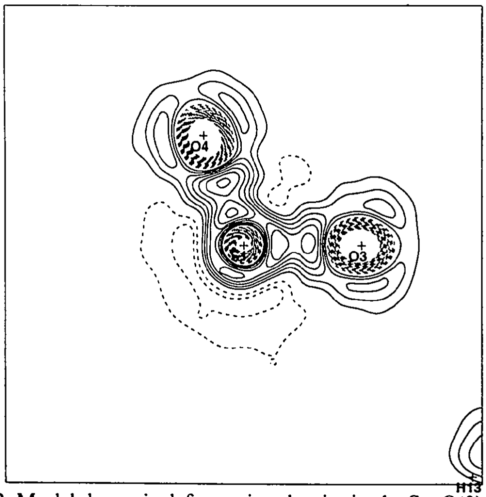

Fig. 12. Model dynamic deformation density in the S—O(3)—O(4) plane. Contours and size as for Fig. 1, resolution 1.09 Å^{-1}.

Fig. 13. Model static deformation density in the S—O(3)—O(4) plane. Contours, size and resolution as for Fig. 12.

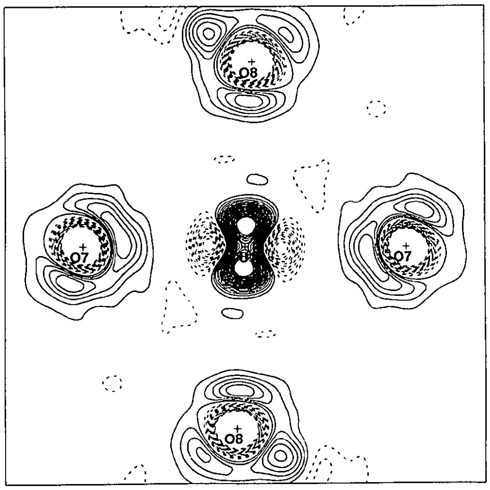

Fig. 14. Model static deformation density in the Cu—O(7)—O(8) plane. Contours, size and resolution as for Fig. 12.

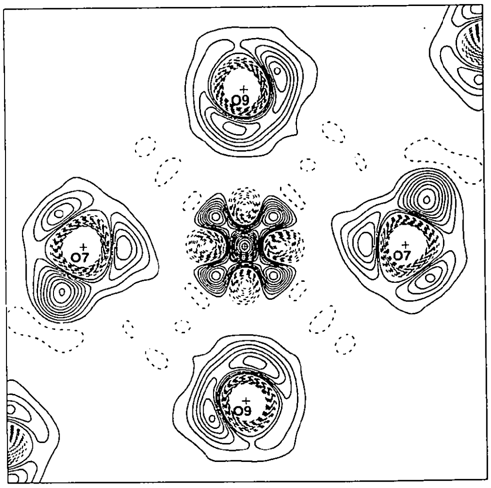

Fig. 15. Model static deformation density in the Cu—O(7)—O(9) plane. Contours, size and resolution as for Fig. 12.

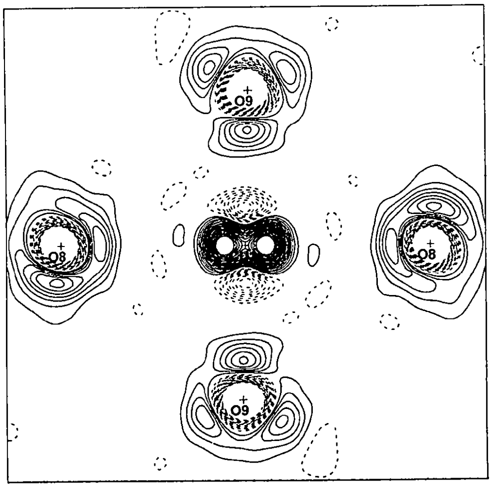

Fig. 16. Model static deformation density in the Cu—O(8)—O(9) plane. Contours, size and resolution as-for Fig. 12.

The model deformation-density maps, as may be inferred from the negligible residual densities, are virtually identical with these. Fig. 12 shows the model deformation density for the S—O(3)—O(4) plane summed up to the experimental resolution of 1.09 Å^{-1}. Fig. 13 shows the corresponding 'static' density map, where thermal motion has been removed. One noticeable feature is that the S—O bonding peak becomes a double maximum. However, we are not confident that this is a real effect. If the peak has a flat top, limitations in the radial flexibility of our model could produce a double peak. We have not shown infinite-resolution maps, since in those, various theoretical assumptions are displayed but are not tested in the experimental data. All the features observed in Fig. 13 are tested against the experiment. Figs. 14–18 show corresponding maps

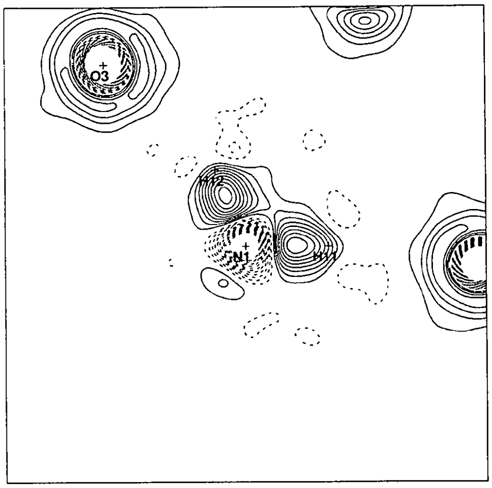

Fig. 17. Model static deformation density in the N—H(11)—H(12) plane. Contours, size and resolution as for Fig. 12.

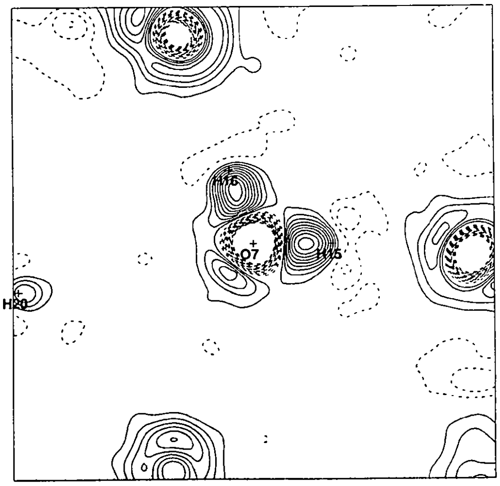

Fig. 18. Model static deformation density in the O(7)—H(15)—H(16) plane. Contours, size and resolution as for Fig. 12.

for Cu—O(7)—O(8), Cu—O(7)—O(9), Cu—O(8)—O(9), N—H(11)—H(12) and O(7)—H(15)—H(16).

In all these maps the various S—O—O, N—H—H and O—H—H planes are all very similar. If there are any deviations, such as might result from different hydrogen-bond arrangements, more detailed analysis will be necessary to reveal them.

The three planes containing the Cu atom are also, almost, planes through the water molecules and perpendicular to the plane bisecting the H—O—H angle. Thus, they contain the two lone pairs of the O atoms.

We also performed a full *X–N* refinement, in which all thermal and positional parameters were fixed at the values determined in the neutron diffraction experiment. The refined values of the parameters hardly alter. The most important parameter, perhaps, the overall scale factor converting from I to F^2, increases by only 0.7%. Thus these deformation-density maps are not significantly different from those of the partial *X–X* analysis. In particular, densities around the nuclear positions, which are very sensitive to the scale factor, are changed little.

Discussion

The molecular geometry and the charge flows which take place in ammonium copper Tutton salt have been discussed previously (Figgis *et al.*, 1992) and are not dealt with further here. There are small but important features revealed by the very low temperature, and the required detailed comparison with theory will be made in a subsequent paper. We do note, however, that, because of the larger radial extent of the D atoms here, following from the use of the 1*s*, $\zeta = 1.0$ exponent compared to the Stewart *et al.* (1965) hydrogen function, and the difference in the effective D-atom positions, fragment charges obtained are not comparable with those from the 85 K X-ray data. In this paper we concentrate on the reliability of the data and the robustness of the modelling.

Comparison of X-ray and neutron diffraction results

We have seen that, in order to reconcile high- and low-angle data and to obtain a model projection efficiency of unity (*i.e.* the correct number of electrons in the unit cell), we introduced extra radial flexibility for the N and O atoms by adding diffuse functions. Before this addition the X-ray diagonal thermal parameters exceeded the neutron values consistently by ~0.001 Å^2, or about 20%. After the introduction of the diffuse functions the agreement was much improved. The positional parameters are statistically indistinguishable between the X-ray and the neutron diffraction data. The ratio of difference to e.s.d. in Table 1 does not exceed 2.8 in any case. The thermal parameters also agree much better, as shown in Table 2. The ratios of the mean values of the thermal parameters from the neutron and X-ray data are 1.01, 0.98 and 1.10 for U_{11}, U_{22} and U_{33}, respectively. If we remember that, at 9 K, the thermal-parameter values are small, this agreement is satisfactory. It corresponds to a mean difference between the two experiments of only 0.0003 Å^2.

However the differences between X-ray and neutron experimental results, even if small, *are* significant. While U_{11} and U_{22} agree, U_{33} is consistently larger for the X-ray experiment, and the moduli of the off-diagonal elements are smaller. Even at 9 K there evidently remain some uncorrected systematic errors.

Temperature and thermal motion

We are interested in two related questions about the thermal motion. Firstly, how does this 9 K X-ray data compare with that at 85 K, and secondly, the validity of the extrapolation from a dynamic to the static model. If we can predict the 85 K deformation densities from those at 9 K, taken with the neutron diffraction data, then we can be confident of the extrapolation from the 9 K dynamic to the static densities.

As illustrated in Figs. 19–21, when we increase thermal motion by using H in place of D and 85 in place of 9 K the changes in the maps are small. The peak and hole heights are reduced about 30%. Hermansson (1984) has already calculated that, for hydrogeneous water, there should be little gain in reduction from liquid-nitrogen temperature to that of liquid helium. We also note that zero-point

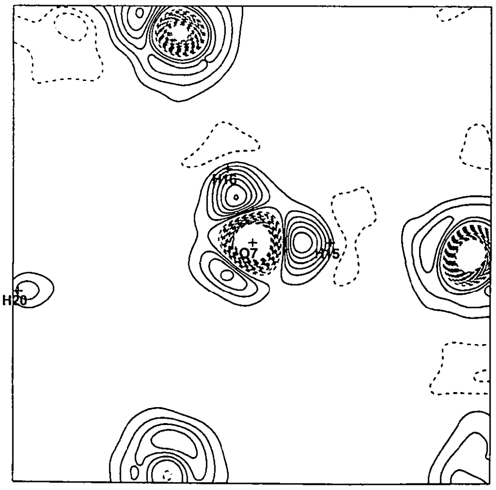

Fig. 19. Model dynamic deformation density in the O(7)—H(15)—H(16) plane; deuteriated water. Contours, size and resolution as for Fig. 12, $T = 9$ K.

motion for D is expected to be about half that for H, and to be attained at lower temperatures. The effect of deuteration will be most noticed at the lowest temperatures. On this basis liquid-helium temperature experiments are preferable to those at liquid-nitrogen temperatures, but the gain is a reduction in thermal motion by less than a factor of 2 for the D, and about 3 for non-D sites.

However, there are equally, or perhaps more, important gains from the use of very low temperatures: they are from the reduction in TDS and anharmonicity. The reduction in these systematic errors improves the reliability of the X-ray data considerably, although the effects are not seen in a marked reduction in the errors of positional and thermal parameters. Also, the resulting ability to use fully data from a neutron diffraction experiment along with the X-ray experiment increases the power of the combined experiments greatly.

When we compare our present maps with the earlier *X–X* maps (Figgis *et al.*, 1992), for example Figs. 22 and 23, there is obviously much less detail in the latter. The difference, however, is not primarily a temperature effect but is mainly as a result of the use of neutron positional parameters, with small contributions from more flexible radial modelling. We demonstrate this in Fig. 23, where we use their *X–X* model on the present 9 K data. This model causes

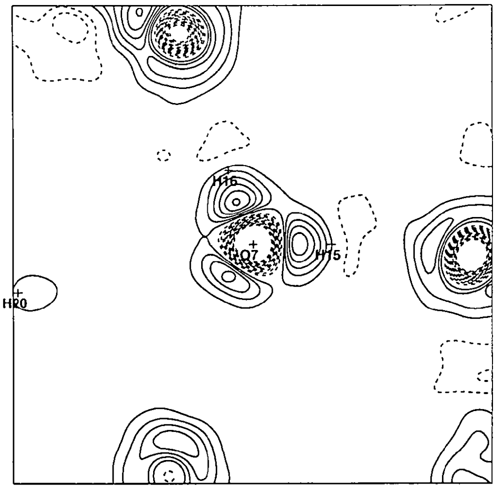

Fig. 20. Model dynamic deformation density in the O(7)—H(15)—H(16) plane; hydrogenous water. Contours, size and resolution as for Fig. 12, $T = 9$ K.

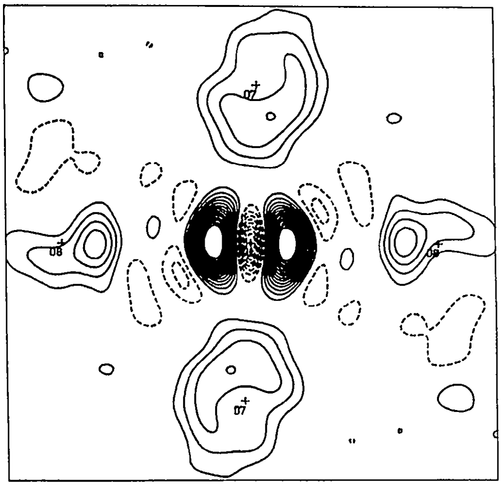

Fig. 22. Experimental deformation density in the Cu—O(7)—O(8) plane. Contours, size and resolution as for Fig. 1, $T = 85$ K. Old '*X–X*' model (Figgis *et al.*, 1992).

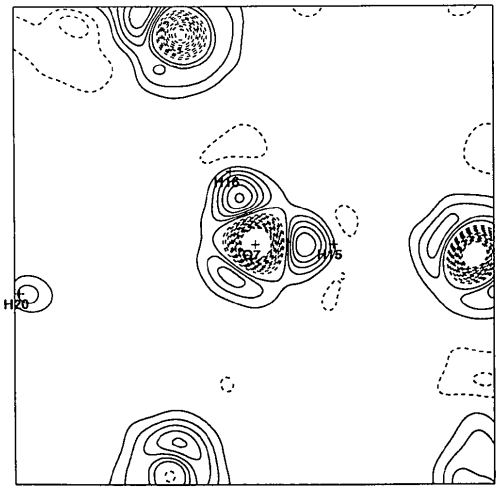

Fig. 21. Model dynamic deformation density in the O(7)—H(15)—H(16) plane; deuteriated water. Contours, size and resolution as for Fig. 12, $T = 85$ K.

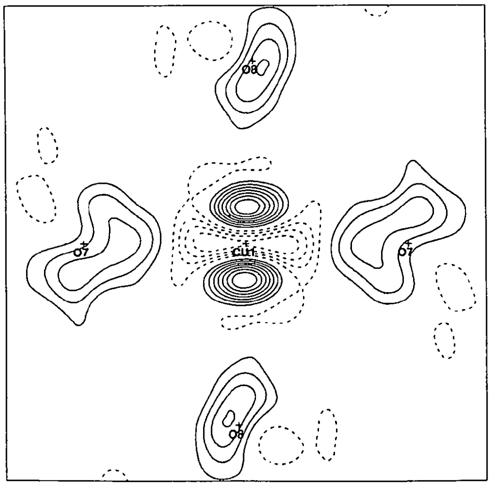

Fig. 23. Experimental deformation density in the Cu—O(7)—O(8) plane. Contours, size and resolution as for Fig. 1, $T = 9$ K. Old '*X–X*' model (Figgis *et al.*, 1992).

radical changes in Fig. 2, but the maps at 85 K (Fig. 22) and 9 K (Fig. 23) are now very similar, except around the Cu site where, as a result of the anharmonicity at 85 K, comparison cannot be quantitative. The density around the water molecules is very similar. We conclude that it is the *X–N* modelling at 9 K that reveals the extra detail. At 85 K such modelling relies on unfounded assumptions about equality of TDS between the two experiments and the absence of anharmonicity (Reynolds *et al.*, 1991).

The good correspondence of the 85 and 9 K deformation maps, when similar models are used, and the agreement of the charge-model-refined parameters, lends support to the validity of extrapolation of the 9 K data to a static density. We note this extrapolation involves removal of thermal motion for the non-D atoms corresponding to about $\frac{1}{3}$ of the increase from 9 to 85 K.

Deformation densities and ab initio calculations

Because of the much smaller extrapolation range needed, and the reduction in systematic errors discussed above, in the 9 K data compared to that at 85 K, errors are much reduced when we compare the results of *ab initio* calculations with the static model densities derived from the experiment. We shall examine this area in detail elsewhere, but remark here that the comparison cannot be more than semi-quantitative. For a quantitative comparison, which may reveal further Cu–water and hydrogen-bonding details, we shall need to compare the experimental structure factors with those derived directly from suitable *ab initio* calculations.

Errors. The errors in our static maps could be estimated from the errors in the structure factors in the normal way. However, we note that there is significant deformation density in regions far from bonding and atomic areas. This should be very small. The values in the static model maps reach up to just over 0.1 e Å^{-3}. We can regard these features as an estimate of the maximum value of the total of statistical and systematic error in regions far from the nuclei, and they may be a better assessment of the limitations in the interpretation of the data. This corresponds to an e.s.d. of ~ 0.04 e Å^{-3}. At the other extreme, the error at the nucleus is dominated by the error of ~ 0.7% in scale factor. We derive this estimate from the change in the scale factor encountered in going from the most primitive (superposition of atoms) model to the best model and also from variation as high- and low-angle data are used. At the resolution of the experiment the O and N nuclei reach total densities of ~ 20 e Å^{-3}, with substantially more at Cu and S. We estimate the e.s.d. at the nuclei as better than 0.2 at O and N, and ~ 0.4 e Å^{-3} for S and Cu.

Table 3. *Valence-function populations around the* Cu *site*

	9 K	85 K	Theory*
$3d-xy$	2.14 (2)	1.58 (6)	1.95
$-xz$	2.02 (2)	2.12 (3)	1.96
$-yz$	2.01 (2)	$= xz$	1.96
$-x^2-y^2$	1.26 (2)	0.82 (7)	1.23
z^2	2.07 (2)	2.18 (6)	1.98
Mixing z^2/x^2-y^2	0.08 (4)	—	--
Radius $3d$	0.998 (3)	1.03 (1)	—
$4p-x$	−0.29 (32)	−0.19 (10)	0.18
$-y$	0.50 (32)	$= x$	0.18
$-z$	0.12 (30)	0.22 (17)	0.11

* Chandler *et al.* (1992).

Electronic configuration of Cu. The multipoles used in the new model correspond to orthorhombic symmetry with axes defined by the O-atom ligand directions. The negligible residuals in the maps confirm both the previous 85 K data and ESR results (Mabbs & Porter, 1973) in their conclusion that this symmetry is appropriate for the electronic density at the Cu site. In orthorhombic symmetry a simple description of the multipoles as $3d$ functions exists. We list these in Table 3, together with the 85 K results, in which tetragonal symmetry was assumed, and results of theoretical calculations (Chandler *et al.*, 1992).

In view of the relevant Cu—O distances [Cu—O(8) $= z$, 2.3002 (5), Cu—O(7) $= x$, 2.0093 (4), and Cu—O(9) $= y$, 1.9607 (4) Å] then the appearance of a hole in the $3d_{x^2-y^2}$ orbital as a result of the large Jahn–Teller lengthening of O(8) is both expected and observed. We note that at 9 K some anomalous features at 85 K have been removed. They are: (1) the low $3d_{xy}$-orbital population; (2) the $3d_{x^2-y^2}$ population below 1.00; and (3) the net negative $4p$-orbital population.

These systematic errors probably arise from the large anharmonicity at the Cu site at that temperature. All have disappeared from the 9 K results, which gives a practical demonstration of the advantages of performing the charge-density experiment at liquid-helium temperatures. Further, e.s.d.'s asociated with the $3d$-orbital populations are much improved. The $4p$ population e.s.d.'s are poorer, but this is as a result of the overlap with the newly introduced diffuse O functions, and exposes the need for examination of total density rather than that of fragments. Accordingly, we do not discuss the copper–water bonding further here, except to note that the σ bonding into the $3d_{x^2-y^2}$ orbital expected theoretically is observed clearly in the experiment.

Water, ammonium, and sulfate-ion deformation densities. With fourth-order multipoles involved in the new modelling, we must make a comparison of the experimental results with theoretical total densities rather than, as in the previous model, with atom fragments. Decomposition of the density by least-squares analysis does not produce 'atomic charges' of sufficient meaning to do justice in a comparison with, say, a Mulliken population analysis.

We show *ab initio* deformation-density maps for the H_2O, NH_4^+ and SO_4^{2-} units in Figs. 24–26 (Chandler & Wajrak, unpublished work). We note the agreement with the corresponding model static deformation maps (Figs. 13, 17 and 18); the main features are reproduced well. We note the deep holes at the O, N and S nuclei, the large peaks in the S—O, N—H and O—H bonds, the lone pairs on the water and sulfate O atoms, and the regions of negative density beyond the O—H and N—H bonds and at larger distances from S, but not along the S—O bonds.

In maps derived from experimental data, deep holes at nuclei are conventionally ignored, for the good reason that the scale factor is likely to be inaccurate by more than 1%. Scale and thermal-parameter errors usually produce very large errors in the density near nuclei. However here, we reiterate, the very low thermal motion smears deep holes but little, and the use of more flexible radial functions allows the modelling of deep holes near nuclei and peaks further away. We also have here a scale factor several times more precise than is usual, following from the better modelling, the full use of neutron data, and more intense data at higher wavevector as a result of reduced thermal motion. The extrapolated, static, hole depths in Figs. 13–18 on O(7) to O(9) are −2.9 (2) to −3.1 (2), on O(3) to O(6) −2.8 (2) to −3.0 (2), for S −1.8 (4) and for N −1.1 (2) e Å^{-3}. These values are significant. They are comparable with the 3*d* valence features around Cu of *ca* +2 and −1 e Å^{-3}, and the O—H and N—H bond peaks of 0.9 to 1.0 e Å^{-3}. These cannot be directly compared to the theoretical hole depths because of the finite (1.09 Å $^{-1}$) resolution of the experimental maps and the thermal smearing.

If we compare Figs. 18 and 24 for the water molecules we see three main features in each, besides the hole at the O-atom nucleus. There is a bonding density reaching a height of 0.9 experimentally and 0.7 e Å^{-3} in the theory. Beyond this, along the O—H vector, is a shallow hole of *ca* −0.1 e Å^3 in both experiment and theory. Lastly there are lone-pair densities of 0.4 and 0.5 e Å^{-3}, respectively, for experiment and theory. In between the lone-pair and bonding densities both theory and experiment show, at that distance from the O atom, that the deformation density reaches zero.

Comparing Figs. 17 and 25 for the ammonium fragment, we also see maxima in the N—H bonds (0.9 experiment and 0.7 e Å^{-3} theory) with shallow holes further out. However, the hole of −0.2 e Å^{-3} behind the N—H bond in the theory does not appear in the experiment.

Figs. 13 and 26 for the sulfate fragment show similar features – bond maxima (0.6 experiment,

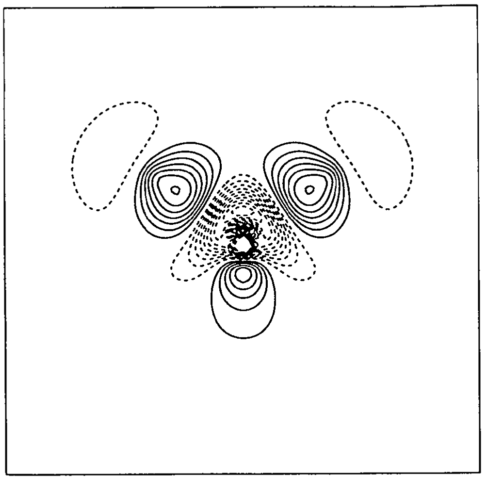

Fig. 24. *Ab initio* theoretical deformation-density map for H_2O. Contours and size as for Fig. 1.

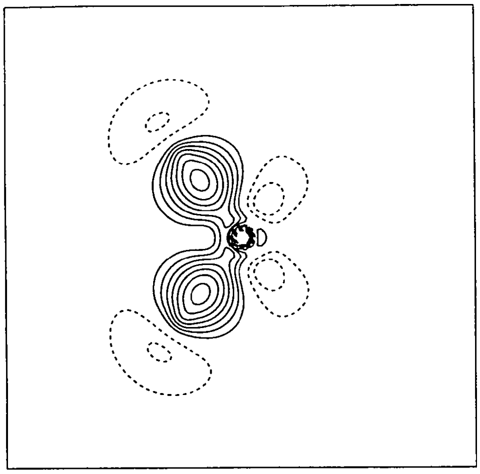

Fig. 25. *Ab initio* theoretical deformation-density map for the NH_4^+ ion. Contours and size as for Fig. 1.

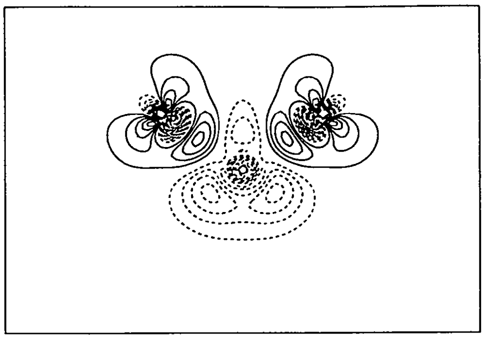

Fig. 26. *Ab initio* theoretical deformation-density map for the SO_4^2 ion. Contours and size as for Fig. 1.

$0.4\,e\,Å^{-3}$ theory), lone pairs (0.4 and $0.5\,e\,Å^{-3}$), holes behind the S—O bonds (-0.3 and $-0.4\,e\,Å^{-3}$). However, in addition, there are differences around the sulfur atoms. The experiment shows a ring of excess density, peaking in the S—O bond and behind it, which does not appear in the theory. While, as previously mentioned, the double nature of the peak of the S—O bond may be an artefact of the modelling, the feature of a rather flat maximum, stretching close to the sulfur site is real and is clearly different from theory. The theoretical treatment does not contain polarization functions of f symmetry in the sulfur atom. An f_{xyz} orbital would be required to generate the peak which is observed.

A more detailed comparison of experiment and theory must be made directly between the observed, thermally smeared, deformation density and similarly treated theoretical densities, rather than attempting to remove thermal motion from the experiment by this model-dependent method. In a subsequent paper we shall attempt this.

BNF and PAR are grateful to the Australian Research Council for financial support.

References

Becker, P. J. & Coppens, P. (1974). *Acta Cryst.* A30, 129–147.

Chandler, G. S., Christos, G. A., Figgis, B. N. & Reynolds, P. A. (1992). *J. Chem. Soc. Faraday Trans.* 2, **88**, 1961–1969.

Clementi, E. & Roetti, C. (1974). *At. Data Nucl. Data Tables*, **14**, 177–478.

Condon, E. V. & Shortley, G. H. (1957). *The Theory of Atomic Spectra*, pp. 158–186. Cambridge Univ. Press.

Coppens, P., Guru-Row, T. N., Leung, P., Stevens, E. D., Becker, P. & Yang, Y. W. (1979). *Acta Cryst.* A35, 63–72.

Coppens, P., Leiserowitz, L. & Rabinovich, D. (1965). *Acta Cryst.* **18**, 1035–1038.

Cromer, D. T. & Liberman, D. (1970). *J. Chem. Phys.* **53**, 1891–1898.

Figgis, B. N., Khor, L., Kucharski, E. S. & Reynolds, P. A. (1992). *Acta Cryst.* B48, 144–151.

Figgis, B. N., Kucharski, E. S. & Reynolds, P. A. (1989). *Acta Cryst.* B45, 232–240.

Figgis, B. N., Reynolds, P. A. & White, A. H. (1987). *J. Chem. Soc. Dalton Trans.* pp. 1737–1745.

Figgis, B. N., Reynolds, P. A. & Williams, G. A. (1980). *J. Chem. Soc. Dalton Trans.* pp. 2339–2347.

Figgis, B. N., Reynolds, P. A. & Wright, S. (1983). *J. Am. Chem. Soc.* **105**, 434–440.

Henriksen, K., Larsen, F. K. & Rasmussen, S. E. (1986). *J. Appl. Cryst.* **19**, 390–394.

Hermannson, K. (1984). Doctoral Thesis, Univ. of Uppsala, Sweden.

Iversen, B. B., Larsen, F. K., Figgis, B. N. & Reynolds, P. A. (1993). *Acta Cryst.* B49. In preparation.

Kissel, L. & Pratt, R. H. (1990). *Acta Cryst.* A46, 170–175.

Lehmann, M. S. & Larsen, F. K. (1974). *Acta Cryst.* A30, 580–584.

Le Page, Y. & Gabe, L. J. (1979). *Acta Cryst.* A35, 73–78.

Mabbs, F. E. & Porter, J. K. (1973). *J. Inorg. Nucl. Chem.* **35**, 3219–3222.

Reynolds, P. A., Figgis, B. N., Kucharski, E. S. & Mason, S. A. (1991). *Acta Cryst.* B47, 899–904.

Stewart, R. F., Davidson, E. R. & Simpson, W. T. (1965). *J. Chem. Phys.* **42**, 3175–3187.

Varghese, J. N. & Mason, R. (1980). *Proc. R. Soc. London Ser. A*, **372**, 1–7.

Weiss, R. J. & Freeman, R. J. (1959). *J. Phys. Chem. Solids*, **10**, 147–161.

Acta Cryst. (1993). B49, 806–811

Electron-Density Distribution in a Crystal of Dipotassium Tetrafluoronickelate, K_2NiF_4

By S. K. Yeh, S. Y. Wu, C. S. Lee and Yu Wang*

Department of Chemistry, National Taiwan University, Taipei, Taiwan

(*Received* 15 *December* 1992; *accepted* 29 *March* 1993)

Abstract

Dipotassium tetrafluoronickelate(II), K_2NiF_4, $M_r = 212.90$, tetragonal, $I4/mmm$, $a = 4.0130\,(6)$, $c = 13.088\,(2)$ Å, $V = 210.78\,(4)$ Å^3, $Z = 2$, $T = 300$ K, $D_x = 3.36$ Mg m^{-3}, Mo $K\alpha$, $\lambda = 0.7107$ Å, $\mu = 656$ mm^{-1}, $F(000) = 204$, final $R = 0.018$ for 698 unique reflections [$I > 2\sigma(I)$]. Charge asphericity around the Ni atom caused by the splitting of $3d$ orbitals is clearly observed in the deformation density. Although the exact site symmetry at the Ni atom is D_{4h}, the local geometry around Ni is practically O_h with Ni—F distances of $2.0065\,(3)$ and $2.0062\,(8)$ Å. The d-orbital occupancies derived from the multipole coefficients are in accordance with the prediction of simple crystal-field theory. The splitting of the d orbitals in D_{4h} is e_g, b_{2g} (from t_{2g} orbitals in O_h), and b_{1g} (from e_g in O_h). The occupancies of all these orbitals are nearly equal with e_g the largest (1.57), b_{1g} and b_{2g} the second largest (1.54), and a_{1g}

---

* To whom all correspondence should be addressed.

Acta Crystallographica Section B
ISSN 0108-7681 © 1993